J Solid State Electrochem (2009) 13:1201–1207
DOI 10.1007/s10008-008-0645-9

ORIGINAL PAPER

System Zn–Rh–O: heat capacity and Gibbs free energy of formation using differential scanning calorimeter and electrochemical cell

Aparna Banerjee · Ziley Singh

Received: 9 May 2008 / Revised: 1 August 2008 / Accepted: 2 August 2008 / Published online: 27 August 2008

Abstract The standard molar Gibbs free energy of formation of $ZnRh_2O_4$(s) has been determined using an oxide solid-state electrochemical cell wherein calcia-stabilized zirconia (CSZ) was used as an electrolyte. The oxide cell can be represented by: $(-)\mathrm{Pt}-\mathrm{Rh}/\{\mathrm{ZnO(s)}+\mathrm{ZnRh_2O_4(s)}+\mathrm{Rh\,(s)}\}//\mathrm{CSZ}//\mathrm{O_2}(p(\mathrm{O_2})=21.21\mathrm{kPa})/\mathrm{Pt}-\mathrm{Rh}\,(+)$. The electromotive force was measured in the temperature range from 943.9 to 1,114.2 K. The standard molar Gibbs energy of formation of $ZnRh_2O_4$(s) from elements in their standard state using the oxide electrochemical cell has been calculated and can be represented by: $\Delta_f G^o\{\mathrm{ZnRh_2O_4(s)}\}/\mathrm{kJmol^{-1}}\ (\pm 1.15) = -744.5 + 0.3487T(\mathrm{K})$. Standard molar heat capacity $C^o_{p,m}(T)$ of $ZnRh_2O_4$(s) was measured using a heat flux-type differential scanning calorimeter in two different temperature ranges, from 127 to 299 and 307 to 845 K. The heat capacity in the higher temperature range was fitted into a polynomial expression and can be represented by: $C^o_{p,m}(\mathrm{ZnRh_2\ O_4, s}, T)\ (\mathrm{J\,K^{-1}mol^{-1}}) = 167.685 + 2.446 \times 10^{-2}T\ (\mathrm{K}) - 33.74339 \times 10^5/T^2\ (\mathrm{K})(307 \le T(\mathrm{K}) \le 845)$. The heat capacity of $ZnRh_2O_4$(s), was used along with the data obtained from the oxide electrochemical cell to calculate the standard enthalpy and entropy of formation of the compound at 298.15 K.

Keywords System Zn–Rh–O · $ZnRh_2O_4$(s) · Gibbs free energy of formation · Enthalpy of formation · Heat capacity · Solid-state electrochemical technique · Thermodynamic functions

A. Banerjee (✉) · Z. Singh
Product Development Section, RC & I Group,
Bhabha Atomic Research Centre,
Mumbai 400 085, India
e-mail: aparnab@barc.gov.in

Introduction

Transparent conductive oxides (TCOs) are those that combine conductivity with optical transparency in the visible region. Doped oxides of In_2O_3(s), SnO_2(s), and ZnO(s) are n-type (electron) conductors, transparent in the visible region. TCOs are widely used as transparent electrodes in flat panel displays [1, 2]. Oxides, exhibiting p-type (hole) conductivity and good optical transparency, were discovered by Kawazoe et al. [3]. TCOs have also been used as transparent metallic electrodes for solar cells and flat panel displays including liquid crystal displays and organic light-emitting diodes (LED) [4]. A combination of the two types of transparent conductors that is n-type and p-type could form a p–n junction. Hence, discovery of p-type TCO has lead to a breakthrough in semiconductors, the "transparent oxide semiconductor" [5]. Transparent oxide semiconductors can be used in innovative devices including UV sensor, UV-LED, and transparent oxide field-effect transistor [6, 7]. Direct patterning of conductive wire is now possible using these oxide semiconductors. Realization of invisible circuits has become within range with a transparent p–n junction [8].

Perovskite and spinel-type oxides of rhodium containing Rh^{+3} are good candidates for p-type wide-gap semiconductors. The band gap originates from the splitting of the d-orbital of the octahedrally coordinated Rh^{+3} ion into fully occupied $t_{2_g}^6$ and empty e_g^0 due to the strong ligand field. Hence, these oxides have a potential application in transparent oxide semiconductors [4]. The band gap observed in spinel-type oxides of rhodium was wider than those in perovskite-type rhodium oxides. $ZnRh_2O_4$(s), a normal spinel with a band gap of 2.1 eV, is a p-type wide-gap semiconductor. This material is transparent in the visible region. The magnetic susceptibility, photoelectron

spectroscopy, and optical measurements of $ZnRh_2O_4(s)$ reveal that the band gap originates from the splitting of d-orbitals [9].

Thermodynamic data like heat capacity, enthalpy of formation, and Gibbs free energy of formation are, however, lacking in the literature. Hence, as part of systematic studies on the thermodynamic properties of compounds in the ternary systems M–Rh–O, measurements have been carried out on the Zn–Rh–O system. Only one ternary oxide $ZnRh_2O_4(s)$ has been reported in the system Zn–Rh–O. The compound has a spinel structure space group Fd3m [10]. Thermodynamics of interoxide compounds are also important for defining the nature of interaction of platinum group metals with refractory oxides and the conditions under which these metals are lost in high temperature processes. Thermodynamic information on these compounds is also useful for assessing their stability in different environments and interactions with support materials [11]. The information is also important for the recovery of precious metals from scrap and from fission products. Hence, it is important to determine physicochemical properties of M–Rh–O systems [12]. Phase diagrams of higher order containing these elements can be readily computed from thermodynamic data on ternary compounds.

In this study, $ZnRh_2O_4(s)$ was synthesized and characterized by X-ray diffraction (XRD). Solid-state electrochemical cells were designed to measure the Gibbs free energy of formation of the ternary oxide $ZnRh_2O_4(s)$ from elements in their standard state in the temperature range from 943.9 to 1,114.2 K. The heat capacity of $ZnRh_2O_4(s)$ was measured in the temperature range from 127 to 845 K using a differential scanning calorimeter (DSC-131). Other thermodynamic parameters were evaluated from these experimental data.

Experimental

Materials

$Rh_2O_3(s)$ was prepared from $RhCl_3(s)$ (Johnson Matthey, England) by passing oxygen over $RhCl_3(s)$ at 1,023 K. This gave α-$Rh_2O_3(s)$, which on further heating at 1,273 K gave the β-phase [13]. For the preparation of $ZnRh_2O_4(s)$, the only compound in the Zn–Rh–O system, stoichiometric proportions of ZnO(s) (mass fraction 0.999, John Baker, Colorado, USA) and $Rh_2O_3(s)$ were mixed, pulverized, and pressed into pellets and calcined at 1,273 K for 2 days. The pellets were reground, pelletized, and heated before the final annealing was done. $ZnRh_2O_4(s)$ having a light brown color was characterized as a pure phase by XRD technique. The values of interplanar spacing *d* obtained in the present study using a STOE diffractometer with Cu Kα radiation (λ=1.5406 Å) with a Ni filter and graphite monochromator is in good agreement with those reported in JCPDS-file number 41-134 [10]. No impurity phase was observed in the XRD pattern. The prepared sample was stored in a desiccator for heat capacity measurements. Phase relations were established by equilibrating various stoichiometric ratios of ZnO(s), $Rh_2O_3(s)$, and $ZnRh_2O_4(s)$ at high temperature and in an inert atmosphere. The phase composition of the samples remained unaltered by equilibration as identified by XRD. Intermetallic phases were not explored. A phase mixture of $\{ZnRh_2O_4(s) + Rh(s) + ZnO(s)\}$ was pelletized and sintered in argon at 1,000 K and used for electrochemical measurements. An isothermal section of the phase diagram for the system Zn–Rh–O at 1,100 K is shown in Fig. 1 and indicates the three-phase region (shown by hashed portion) chosen for the determination of Gibbs free energy by using an oxide solid-state electrochemical cell.

The oxide cell assembly

A double-compartment cell assembly with 0.15-mol fraction calcia-stabilized zirconia (CSZ) solid electrolyte tube with one end closed and flat was used to separate the gaseous environments of the two electrodes. A detailed experimental setup was described in an earlier publication [14]. The dimensions of the CSZ tube used were 13 mm outer diameter, 9 mm inner diameter, and 380 mm in

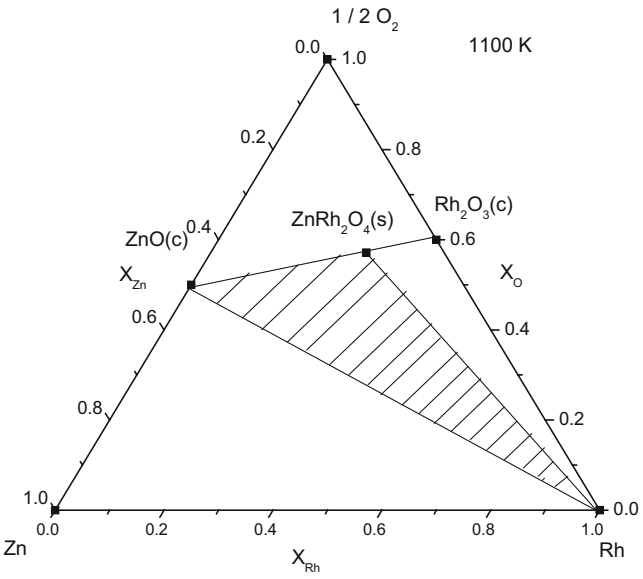

Fig. 1 Isothermal section of the phase diagram for the system Zn–Rh–O at 1,100 K The *hashed portion* indicates the phase field under investigation

length. Argon gas, flowing at a rate of 1 $dm^3\ h^{-1}$, purified by passing it through towers containing the reduced form of the BASF (Akteingesellschaft, Ludiwigshafen, Germany) catalyst, molecular sieves, magnesium perchlorate, and hot uranium metal at 550 K, served as the gaseous atmosphere for the cell. A Faraday cage was placed between the furnace and cell assembly. The cage was grounded to minimize the induced electromagnetic field (e.m.f.) on the cell leads. Alumina-sheathed Pt–40% Rh leads were used to measure the e.m.f. The sample pellet was made by compaction and pelletization of a mixture of $ZnRh_2O_4(s)+ZnO(s)+Rh(s)$ in the ratio of 1:1:1 into pellets of dimension 10 mm diameter and 3 mm thickness at a pressure of 100 MPa. Air was used as the reference electrode because of convenience and good reversibility. The temperature of the cell was measured by a calibrated chromel–alumel thermocouple located in the vicinity of the pellet. The e.m.f. of the cell was measured when the value of the e.m.f. was steady for 2–3 h using a high-impedance Keithley 614 electrometer. Voltages were reproducible in subsequent heating cycles. E.m.f. was measured after equilibrating the galvanic cells at 1,000 K for at least 24 h. The following cell configuration was employed in the present study:

$$(-)\mathrm{Pt-Rh}/\{\mathrm{ZnRh_2O_4(s)+ZnO(s)+Rh(s)}\}//\mathrm{CSZ}//\ \mathrm{O_2}\{p(\mathrm{O_2})=21.21\mathrm{kPa}\}/\mathrm{Pt-Rh}(+) \quad (1)$$

The reversibility of the solid-state electrochemical cell was checked by microcoulometric titration in both directions. A small quantity of current was passed through the cell in either direction. Removal of the applied current returned the cell e.m.f. to its original value. The e.m.f. of the cell was also found to be independent of flow rate of the inert gas passing over the electrodes. The XRD pattern of the sample pellet before and after electrochemical measurements did not reveal any new phases.

Measurement of heat capacity of $ZnRh_2O_4(s)$

Heat capacity measurements were carried out using a heat flux-type differential scanning calorimeter (Model: DSC-131, Setaram Instrumentation, France). The transducer of DSC-131 has been designed using the technology of the plate-shaped DSC rods made of chromel–costantan. It is arranged in a small furnace with a metal resistor of low thermal inertia so as to produce high heating and cooling rates, thereby providing for high-speed experiments. The transducer also possesses very good sensitivity over the entire temperature range (100 to 950 K). The temperature calibration of the calorimeter was carried out in the present study by the phase transition temperature of the National Institute of Standards and Technology (NIST) reference materials (mercury: T_{fus}=234.316 K; gallium: T_{fus}= 302.914 K; indium: T_{fus}=429.748 K; tin T_{fus}=505.078 K; lead: T_{fus}=600.600 K) and analytical reagent-grade samples (*n*-pentane: T_{fus}=140.490; cyclohexane: T_{fus}=280.1 K, T_{trs}= 190.0 K; deionized water: T_{fus}=273.160 K; potassium nitrate: T_{fus}=400.850 K; silver sulfate: T_{fus}=703.150 K; potassium sulfate: T_{fus}=856.150 K). Heat calibration of the calorimeter was carried out from the enthalpies of transition of the reference materials. For the determination of heat capacity, NIST synthetic sapphire (SRM 720) in the powder form was used as the reference material [15]. Temperature calibration and experimental setup for the calorimeter has been described elsewhere [16]. Heat capacity of the oxide was determined in two different temperature ranges: (1) $127 \le T$ (K)≤ 299 and (2) $307 \le T$ (K)≤ 845.

The classical three-step method in the continuous heating mode was followed in this study to measure the specific heat in the first temperature range from 127 to 299 K. Heat flow as a function of temperature was measured at a heating rate of 5 K min^{-1} with high-purity helium as a carrier gas with a flow rate of 2 $dm^3\ h^{-1}$. In order to determine heat capacity in the step-heating mode that is the second temperature range from 307 to 845 K, three sets of experiments were carried out in argon atmosphere at a heating rate of 5 K min^{-1} and a gas flow rate of 2 $dm^3\ h^{-1}$. All three sets of experiment were performed under identical experimental conditions of heating rate, carrier gas flow rate, delay time, and temperature range. Two empty, flat-bottomed cylindrical aluminum crucibles with covering lids (capacity 10^{-4} dm^3) of identical masses were selected for the sample and reference cells.

In the first run, both the sample and reference cells were loaded with empty aluminum crucibles. The heat flow versus temperature was measured at a heating rate of 5 K min^{-1}. In the second run, a known weight of NIST synthetic sapphire (SRM-720) was loaded in the sample cell keeping the crucible in the reference side empty, and once again, the heat flow versus temperature was measured in the same temperature range and at the same heating rate. In the third run, a known weight of the sample of $ZnRh_2O_4(s)$ was loaded in the sample cell, with reference cell being empty, and once again, the heat flow as a function of temperature was measured. About 300–350 mg of the sample was used for the heat capacity measurements. In DSC-131, the heat capacity of the sample under investigation can be calculated by a simple comparison of the heat flow rates in three runs

as illustrated in the literature [17]. For a defined step of temperature, the thermal effect corresponding to the sample heating is integrated. The thermal equilibrium of the sample is reached after each step of temperature. If T_i represents the initial temperature, the temperature interval step is chosen between T_j and T_{j+1}, we define: $T_j=T_i+\Delta T$ and $T_{j+1}=T_i+(j+i)\Delta T$. The expression used for the calculation of heat capacity of the sample is given as:

$$C_p(T_j)_{sample} = \langle (HF_{sample} - HF_{blank}) \rangle / \langle (HF_{Ref} - HF_{blank}) \rangle \times (M_{Ref}/M_{sample}) \times \left\langle C_p(T_j)_{Ref} \right\rangle \quad (2)$$

where, HF_{blank}, HF_{Ref}, and HF_{sample} represent heat flow during the first, second, and third runs, respectively. $C_p(T_j)_{sample}$ and $C_p(T_j)_{Ref}$ represent the heat capacities of sample and reference material in joules per Kelvin per gram, and M_{sample} and M_{Ref} represent the mass of the sample and reference, respectively. The heat capacity thus obtained was then converted to joules per Kelvin per mole. Accuracy of measurements were checked by measuring the specific heat of Fe_2O_3(s) (mass fraction 0.998) in the temperature range from 127 to 845 K, and the values were found to be within ±2% as compared with the literature values [18].

Results

Solid-state electrochemical measurements for the oxide cell

The e.m.f. of the solid-state electrochemical cell is related to the partial pressure of oxygen at the two electrodes and is given by the relation:

$$E=(RT/nF) \int_{p''(O_2)}^{p'(O_2)} t(O^{2-})\, d\ln p(O_2) \quad (3)$$

E is the measured e.m.f. of the cell, R=8.3144 J K^{-1} mol^{-1} is the universal gas constant, n is the number of electrons participating in the electrode reaction, F= 96,486.4 C mol^{-1} is the Faraday constant, T is the absolute temperature, $t(O^{2-})$ is the effective transference number of O^{2-} ion for the solid electrolyte combination and $p'(O_2)$ and $p''(O_2)$ are the equilibrium oxygen partial pressures at the positive and negative electrodes, respectively. The transport number of oxygen ion in the present electrolyte cell arrangement is nearly unity ($t(O^{2-})>0.99$) at the oxygen pressures and temperature range covered in this study. Hence, the e.m.f. of the cell is directly proportional to logarithm of the ratio of partial pressures of oxygen at the electrodes:

$$E = (RT/nF)\ \ln\{p'(O_2)/p''(O_2)\} \quad (4)$$

Thus,

$$nFE = RT \ln\ p'(O_2) - RT \ln\ p''(O_2) \quad (5)$$

The solid-state electrochemical cell configuration is given in Eq. 1.

The half-cell reaction for the cell is given by:

$$3/2\ O_2(g) + 6\,e^- = 3\,O^{2-}(\text{at the cathode}) \quad (6)$$

and

$$ZnO(s) + 2\,Rh(s) + 3\,O^{2-} = ZnRh_2O_4(s) + 6\,e^-\ (\text{at the anode}) \quad (7)$$

The overall cell reaction can be represented by:

$$ZnO(s) + 2\ Rh(s) + 3/2\ O_2(g) = ZnRh_2O_4(s). \quad (8)$$

The least-squares regression analysis of the e.m.f. gives:

$$E/V(\pm 0.00064) = 0.67458 - 4.5018 \times 10^{-4}\ (T/K).(943.9<T/K<1,142.2) \quad (9)$$

The uncertainties quoted are the standard deviation in e.m.f. Variation of e.m.f. as a function of temperature is presented in Fig. 2. The $\Delta_rG^o(T)$ for the reaction given in Eq. 8 involves the transfer of six electrons and can be given by:

$$ZnO(s) + 2Rh(s) + 3/2\ O_2(g) = ZnRh_2O_4(s). \quad (10)$$

$$\Delta_rG^o(T) = -6\,FE = \Delta_fG^o\{ZnRh_2O_4(s)\} - \Delta_fG^o\{ZnO(s)\} - 3/2\ RT\ln p(O_2) \quad (11)$$

Substituting the value of $\Delta_fG^o\{ZnO(s)\}$ from the literature [19] and e.m.f. values from Eq. 9, the standard Gibbs free energy of formation of $ZnRh_2O_4$(s) from elements in their standard state was determined as:

$$\Delta_fG^o\{ZnRh_2O_4(s)\}/kJ\ mol^{-1}\ (\pm 1.11) = -744.5 + 0.3487\ T(K). \quad (12)$$

The error includes the standard deviation in e.m.f. and the uncertainty in the data taken from the literature. The Gibbs free energy of formation is a linear function of temperature within the investigated temperature range, i.e., from 943.9 to 1,114.2 K. The slope and intercept of this least-squares line corresponds, respectively, to the average values of the standard molar enthalpy and entropy of

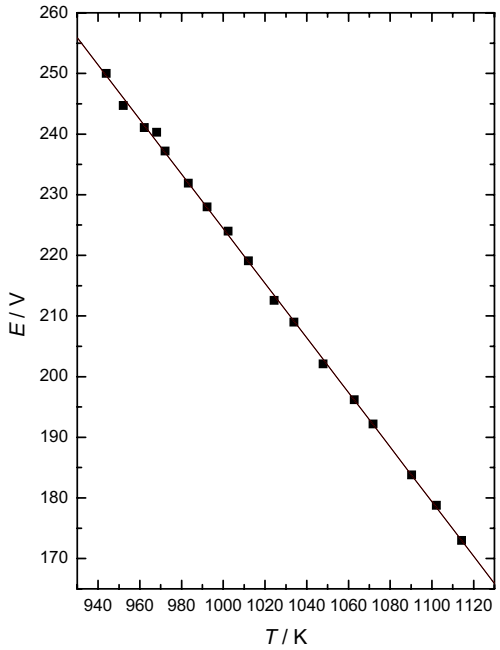

Fig. 2 Variation of e.m.f. of the cell: $(-)\mathrm{Pt}-\mathrm{Rh}/\{\mathrm{ZnRh_2O_4(s)}+\mathrm{ZnO(s)}+\mathrm{Rh(s)}\}//\mathrm{CSZ}//\mathrm{O_2}\{p(\mathrm{O_2})=21.21\mathrm{kPa}\}/\mathrm{Pt}-\mathrm{Rh}(+)$ as a function of temperature

formation of $ZnRh_2O_4$(s) in the temperature range covered by e.m.f. measurements.

Standard molar heat capacity of $ZnRh_2O_4$(s)

The heat capacity values of $ZnRh_2O_4$(s) obtained in the two different temperature ranges (1) $127 \le T$ (K)≤ 299 and (2) $307 \le T$ (K)≤ 845 are tabulated in Tables 1 and 2, respectively. The values of heat capacities are best fitted into the following polynomial expression in the higher temperature range by the least-squares method.

$$C_p^o(\mathrm{ZnRh_2O_4, s}, T)\left(\mathrm{J\ K^{-1}\ mol^{-1}}\right) = 167.685 + 2.446 \times 10^{-2} T(\mathrm{K}) - 33.74339 \times 10^5 / T^2(\mathrm{K}). \quad (13)$$

The heat capacity data for $ZnRh_2O_4$(s) at 298.15 K has been reported for the first time.

Enthalpy and entropy of formation

The enthalpy of formation of $ZnRh_2O_4$(s) at 298.15 K has been calculated by the second law method. Heat capacity data obtained in this study by using a differential scanning calorimeter along with transition enthalpies of Rh(s) [19], Zn(s), and O_2(g) [21] were used to determine the value of $\Delta_f H^o$ ($ZnRh_2O_4$,s, 298.15 K) and was found to be -760.116 kJ mol^{-1}. From the heat capacity measurements and the entropy at the average experimental temperature, the standard molar entropy S^o (298.15 K) for this compound was calculated to be S_m^o {$ZnRh_2O_4$,s, 298.15 K}=141.4 J K^{-1} mol^{-1}. The entropy at 298.15 K estimated by the Latimer entropy contribution of individual ions [20] gives S^o (298.15 K)=147.8±6.3 J K^{-1}mol^{-1} for $ZnRh_2O_4$(s). Based on the calculated value of entropy and the measured heat capacity, the derived thermodynamic functions of $ZnRh_2O_4$(s) were calculated, and the resulting values were extrapolated to 1,000 K and given in Table 3.

Table 1 Low temperature standard molar heat capacity of $ZnRh_2O_4$(s)

T (K)	C_p (J K^{-1} mol^{-1})	T (K)	C_p (J K^{-1} mol^{-1})	T (K)	C_p (J K^{-1} mol^{-1})
126.9	59.3	184.0	106.6	242.8	121.2
129.9	64.7	187.1	107.6	245.9	121.8
132.7	68.7	190.2	108.6	249.0	122.5
135.6	72.7	193.2	109.6	252.2	123.0
138.7	76.1	196.3	110.6	255.3	123.7
141.7	79.4	199.4	111.3	258.4	124.2
144.7	82.5	202.5	111.9	261.5	124.8
147.7	85.1	205.6	112.6	264.6	125.3
150.6	87.5	208.7	113.6	267.7	125.9
153.6	89.8	211.8	114.2	270.9	126.6
156.6	92.2	214.9	114.6	274.0	127.5
159.7	94.2	218.0	115.3	277.1	128.6
162.7	96.2	221.1	116.0	280.2	129.4
165.7	98.2	224.2	116.8	283.4	130.1
168.7	99.9	227.3	117.6	286.5	131.0
171.8	101.2	230.4	118.4	289.6	132.0
174.9	102.9	233.5	119.1	292.7	133.1
177.9	104.2	236.6	119.9	295.9	134.2
181.0	105.6	239.7	120.6	299.0	135.0

Table 2 High-temperature standard molar heat capacity of $ZnRh_2O_4$(s)

T (K)	C_p (J K^{-1} mol^{-1})	T (K)	C_p (J K^{-1} mol^{-1})
307.3	138.3	584.8	171.9
326.7	144.9	604.8	173.0
346.2	148.4	624.8	174.0
365.8	151.3	644.8	175.1
385.5	154.2	664.9	176.0
405.3	157.1	684.9	176.9
425.2	159.7	704.9	177.8
445.2	162.0	725.0	178.6
465.2	163.9	745.0	179.6
485.1	165.6	765.1	180.6
505.0	167.0	785.2	181.6
524.9	168.3	805.2	182.6
544.9	169.5	825.3	183.5
564.9	170.7	845.3	184.0

Table 3 Derived thermodynamic functions of $ZnRh_2O_4$(s)

T (K)	$H^o_T - H^o_{298.15}$	C^o_p	$S^o(T)$ (J mol^{-1} K^{-1})	fef^a (J mol^{-1} K^{-1})
300.0	261.4	137.6	142.3	141.4
350.0	7,439.3	148.8	164.4	143.8
400.0	15,080.6	156.5	184.8	147.1
450.0	23,051.3	162.1	203.5	152.3
500.0	31,271.1	166.5	220.8	158.3
550.0	39688.9	170.9	236.9	164.7
600.0	48,270.6	173.8	251.8	171.4
650.0	56,992.7	175.7	265.8	178.1
700.0	65,838.1	178.6	291.2	184.8
750.0	74,794.7	180.2	302.9	191.5
800.0	83,853.1	182.1	314.0	198.1
850.0	93,006.2	183.9	324.6	204.6
900.0	102,248.5	185.7	334.7	210.9
950.0	111,575.7	187.4	344.3	217.2
1,000.0	120,984.3	188.9	353.6	223.4

fef^a $=-(G^o(T)-H^o(298.15\ K))/T$

Oxygen potential diagram

In an isothermal oxygen potential diagram, the phase relations are represented as a function of partial pressure of oxygen. The oxygen potential diagram for the system Zn–Rh–O at T=1,100 K, computed from the results of this study, is shown in Fig. 3. The composition variable is the cationic fraction $\eta_{Rh}/(\eta_{Rh}+\eta_{Zn})$ where η_i represents moles of component i. Oxygen is not included in the composition parameter. The diagram provides useful information on the oxygen potential range for the stability of various phases. The diagram is complementary to the conventional Gibbs triangle representation of phase relations in ternary systems, where the composition of each phase can be unambiguously displayed [13]. All the topological rules of construction for conventional binary temperature–composition phase diagrams are applicable to the oxygen potential diagram shown in Fig. 3. When three condensed phases coexist at equilibrium in a ternary system such as Zn–Rh–O, the system is bivariant; at a fixed temperature and total pressure, three condensed phases can coexist only at a unique partial pressure of oxygen. Therefore, horizontal lines on the diagram represent three phase equilibria [22]. A similar diagram at other temperatures can be readily computed from the thermodynamic data. Phase relations can also be computed as a function of temperature at constant oxygen partial pressures. The computed phase diagram in air (p_{O2}=2.12×10^4 Pa) is shown in Fig. 4.

Conclusion

Zinc rhodium (III) oxide was synthesized by the solid-state reaction route and characterized by the XRD method. The electromotive force was measured as a function of temperature using a solid-state electrochemical cell in the

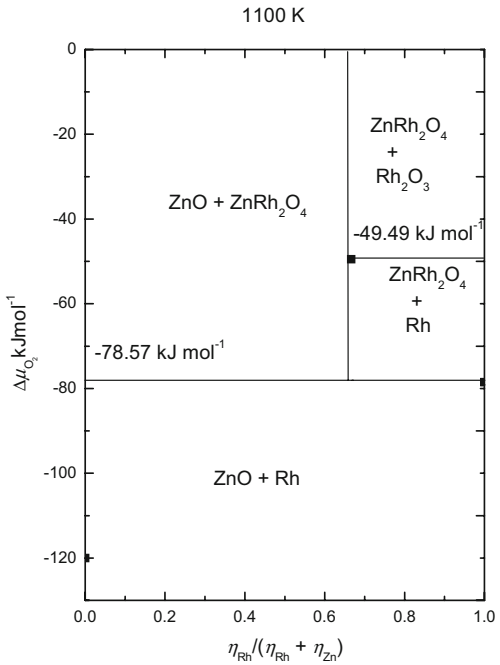

Fig. 3 Oxygen chemical potential diagram for the system Zn–Rh–O at 1,100 K

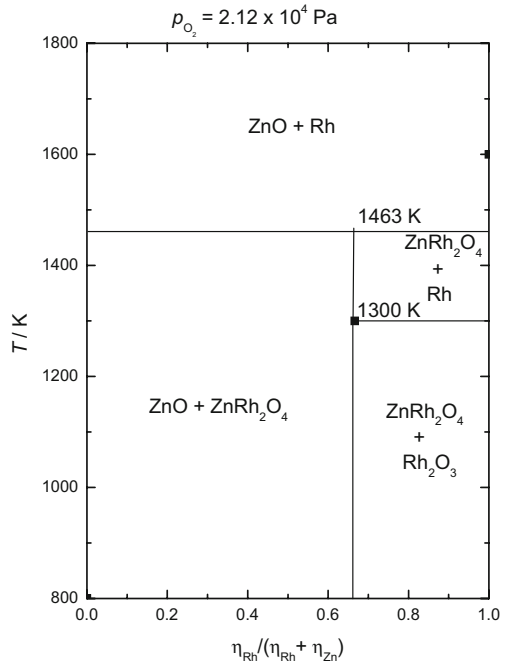

Fig. 4 Temperature–composition phase diagram for the system Zn–Rh–O at oxygen partial pressure of 2.12×10^4 Pa

temperature range from 943.9 to 1,114.2 K. The Gibbs free energy of formation of $ZnRh_2O_4$(s) from elements in their standard state can be given by $\Delta_f G^o(ZnRh_2O_4,T,s)$ (kJ $mol^{-1}\pm1.11)=-744.5+0.3487T$ (K). Standard molar heat capacity of $ZnRh_2O_4$(s) is: $C_p^o(ZnRh_2O_4,s,T)$(J K^{-1} mol^{-1})= $167.685+2.446\times10^{-2}T$ (K)$-33.74339\times10^5/T^2$ (K). The second law method gave the value of $\Delta_f H^o(ZnRh_2O_4$, s,298.15 K) and $S_m^o\{ZnRh_2O_4$,s, 298.15 K} as −760.116 kJ $mol^{-1}$and 141.4 J K^{-1} mol^{-1}, respectively. The Gibbs free energy of formation and the heat capacity of zinc rhodium (III) oxide were determined and reported for the first time, and no other experimental data are available in the literature for comparison.

Acknowledgments The authors wish to thank Dr. N. D. Dahale, for XRD analysis. The authors are thankful to Dr. V. Venugopal, Group Director, RC and I Group, and Shri B.K. Sen, Head, Product Development Section, RC and I Group, for their constant support and encouragement.

References

1. Hamberg I, Granquist CG (1986) J Appl Phys 60:123. doi:10.1063/1.337534
2. Chopra KL, Major S, Pandya DK (1983) Thin Solid Films 102:1. doi:10.1016/0040-6090(83)90256-0
3. Kawazoe H, Yasukawa M, Hyodo H, Kurita M, Yanagi H, Hosono H (1997) Nature 389:939. doi:10.1038/40087
4. Ginley DS, Bright C (2000) MRS Bulletin 25-(8)
5. Ohta H, Nomura K, Hiramatsu H, Ueda K, Kamiya T, Hirano M et al (2003) Solid-State Electron 47:2261. doi:10.1016/S0038-1101(03)00208-9
6. Ohta H, Kawamura K, Orita M, Hirano M, Sarukura N, Hosono H (2000) Appl Phys Lett 77:475. doi:10.1063/1.127015
7. Ohta H, Orita M, Hirano M, Hosono H (2001) J Appl Phys 89:5720. doi:10.1063/1.1367315
8. Thoman G (1997) Nature 389:907. doi:10.1038/39999
9. Mizoguchi H, Hirano M, Fujitsu S, Takeuchi T, Ueda K, Hosono H (2002) Appl Phys Lett 80:1207. doi:10.1063/1.1450252
10. Schulz E (1989) Mineral-Petrographisches Institut der Univ., Heidelberg, Germany, ICDD Grant-in-aid.
11. Jacob KT, Okabe TH, Uda T, Waseda Y (1999) Bull Mater Sci 22:741. doi:10.1007/BF02745598
12. Kayanuma Y, Okabe TH, Mitsuda Y, Maeda M (2004) J Alloys Compd 365:211. doi:10.1016/S0925-8388(03)00666-2
13. Jacob KT, Waseda Y (2000) J Solid State Chem 150:213. doi:10.1006/jssc.1999.8588
14. Banerjee A, Prasad R, Venugopal V (2004) J Alloys Compds 381:58. doi:10.1016/j.jallcom.2004.03.105
15. Sabbah R, Xu-Wu A, Chickos JS, Planas Leitao ML, Roux MV, Torres LA (1999) Thermochim Acta 331:93. doi:10.1016/S0040-6031(99)00009-X
16. Parida SC, Rakshit SK, Dash S, Singh Z, Prasad R, Venugopal V (2004) J Chem Thermodyn 36:911. doi:10.1016/j.jct.2004.06.011
17. Hohne GWH, Hemminger WF, Flammershein HJ (2003) Differential scanning calorimetry, 2nd edn. Springer, Berlin
18. Chase MW Jr (1998) JANAF thermochemical tables, monograph no. 91995, 4th edn. ACS, AIP, NIST, Washington, DC
19. GTT Technologies (2004) FactSage, version 5.3.1 (1976–2004) Thermo-chemical database software, thermfact, GTT Technologies, Germany
20. Kubachewski O, Alcock CB, Spencer PJ (1993) Materials thermochemistry, 6th edn. Pergamon, Oxford
21. Graves K, Kirby B, Rardin R (1991) FREED version 2.1.
22. Pankratz LB (1982) Thermodynamic properties of elements and oxides, Bulletin 672. US Bureau of Mines